Generation of a precise time scale assisted by a near-continuously operating optical lattice clock

Takumi Kobayashi,[1,*,§] Daisuke Akamatsu,[2,§] Kazumoto Hosaka,[1] Yusuke Hisai,[2,‡] Akiko Nishiyama,[1] Akio Kawasaki,[1] Masato Wada,[1] Hajime Inaba,[1] Takehiko Tanabe,[1] Tomonari Suzuyama,[1,†] Feng-Lei Hong,[2] and Masami Yasuda[1]

[1] *National Metrology Institute of Japan (NMIJ), National Institute of Advanced Industrial Science and Technology (AIST), 1-1-1 Umezono, Tsukuba, Ibaraki 305-8563, Japan*

[2] *Department of Physics, Graduate School of Engineering Science, Yokohama National University, 79-5 Tokiwadai, Hodogaya-ku, Yokohama 240-8501, Japan*

(Received 2 January 2024; accepted 16 April 2024; published 7 June 2024)

We report on the achievement of a reduced time difference in a time scale with respect to Coordinated Universal Time (UTC) by steering a hydrogen-maser-based time scale with a near-continuously operating optical lattice clock. The time scale is generated in a postprocessing analysis for 230 days using a hydrogen maser with its fractional frequency stability limited by a flicker floor of 2×10^{-15} and an Yb optical lattice clock operated with an uptime of 81.6%. During the 230-day period, the root-mean-square time difference of our time scale with respect to UTC is 0.52 ns, which is a better performance than those of time scales steered by microwave fountain clocks, which exhibit root-mean-square differences from 0.99 to 1.6 ns. With the high uptime achieved by the Yb optical lattice clock, our simulation results indicate the potential for generating a state-of-the-art time scale with a time difference of <0.1 ns over a month using a better hydrogen maser reaching the mid-10^{-16} stability level. This work demonstrates that the use of an optical clock with a high uptime enhances the stability of a time scale.

DOI: 10.1103/PhysRevApplied.21.064015

I. INTRODUCTION

The generation of a time scale is an essential mission of national metrology institutes for time keeping and frequency calibration services for various industries; it is also crucial for navigation, telecommunication, and new potential applications, including geodesy [1,2] and studies in fundamental physics [3–11]. A time scale is generated by a continuously running flywheel oscillator with its frequency steered by an atomic frequency standard. As a global time scale, the Bureau International des Poids et Mesures (BIPM) computes International Atomic Time (TAI) and Coordinated Universal Time (UTC), which are generated by several hundreds of microwave flywheel clocks around the world and steered by Cs and Rb microwave clocks and Yb and Sr optical lattice clocks that are officially approved as primary and secondary frequency standards [12,13]. A national institute k generates its official local time scale UTC(k) by synchronizing a local flywheel to UTC using time-comparison data obtained via a satellite link. For example, the National Metrology Institute of Japan (NMIJ) maintains UTC(NMIJ) within several tens of nanoseconds from UTC in this way.

The time difference of UTC(k) with respect to UTC is expected to be reduced by locally realizing a time scale based on a primary or secondary frequency standard instead of referencing only UTC, since the time-comparison data between UTC and UTC(k) are provided by BIPM with a latency of about 1 month. Improvements of UTC(k) in this way have so far been demonstrated by steering flywheel hydrogen masers with Cs or Rb microwave fountain clocks [14–17].

With a view to the redefinition of the SI second [18–20], some institutes have started to incorporate optical clocks in local time scales. The best optical clocks reach fractional frequency stabilities and uncertainties at the 10^{-18}–10^{-19} level [21–28], and they thus have the potential to significantly improve the stabilities of time scales compared with microwave clocks. Since the availabilities of optical clocks are commonly limited to short periods with low uptimes, previous works have mostly relied on microwave [29–35] and optical [36] flywheels with good frequency stability to bridge the gaps in the operation of optical clocks. Among these previous works, long-term generation

*Corresponding author: takumi-kobayashi@aist.go.jp
†Deceased.
‡Present address: Shimadzu Corporation, 3-9-4 Hikaridai, Seika-cho, Soraku-gun, Kyoto 619-0237, Japan.
§These authors contributed equally to this work.

of optical-clock-based time scales for several months has been reported with microwave flywheels, reaching the low-10^{-16} stability level. One example is a time scale based on a hydrogen maser steered by a Sr optical lattice clock operated for 10^4 s per week, which exhibits a time difference of 0.79 ns after 5 months from another stable global time scale TT(BIPM) [30]. Another example is a time scale based on an ensemble of a few hydrogen masers and a few commercial Cs clocks steered by an Yb optical lattice clock with an uptime of 6%, which follows UTC with a root-mean-square time difference of 0.40 ns over 160 days [31]. In the methods described previously, however, the stabilities of time scales are ultimately limited by stochastic fluctuations of the flywheels during the dead time of the optical clocks. Therefore, the continuous operation of an optical clock is desirable to take full advantage of its stability.

For potential applications of optical clocks, including TAI calibration and geodesy, several groups have developed robust optical clocks and reported their operation with high uptimes [37–41] (e.g., 84% for 25 days [37]). So far, the high-uptime operation periods of these clocks have typically lasted for $\lesssim$1 month, which is not long enough for the practical generation of a time scale. However, NMIJ has achieved the operation of an Yb optical lattice clock with an uptime of >80% for many months [42]. Thus, it is worth discussing a method for generating a time scale based on the nearly continuous operation of an optical clock.

In this paper, we report on postprocessing generation of a local time scale UTC(NMIJ)′ for 230 days by steering the frequency of a single hydrogen maser to that of an Yb optical lattice clock operated with an uptime of 81.6% using a Kalman filter algorithm. The root-mean-square time difference of UTC(NMIJ)′ with respect to UTC is 0.52 ns. Although the fractional frequency stability of our hydrogen maser is limited by a flicker floor of 2×10^{-15}, UTC(NMIJ)′ exhibits better performance than time scales based on Cs or Rb fountain clocks. We also simulate the projected performance of UTC(NMIJ)′ with a better flywheel hydrogen maser that reaches a stability of 5×10^{-16}, which implies a time difference of <0.1 ns over a month.

II. METHOD

A. Experimental setup

Figure 1 shows the experimental setup for generating UTC(NMIJ)′. Our current official time scale UTC(NMIJ) is generated by a hydrogen maser HM1 (KVARZ, CH1-75A) and an auxiliary output generator AOG (Symmetricom, AOG-110) for frequency steering. The frequency of UTC(NMIJ) is typically steered once every few months by manually adding the fractional correction frequency $\Delta y^{\mathrm{AOG}} \sim 10^{-15}$ to the frequency of AOG to reduce the

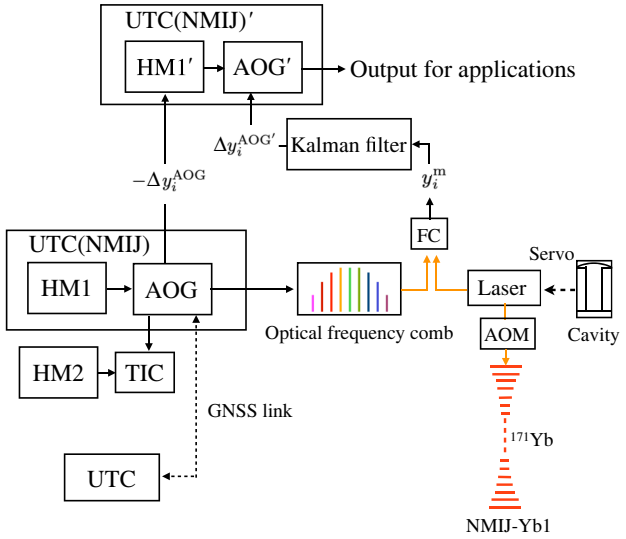

FIG. 1. Experimental setup for generating a local time scale UTC(NMIJ)′ based on the Yb optical lattice clock NMIJ-Yb1. HM: hydrogen maser, AOG: auxiliary output generator, AOM: acousto-optic modulator, FC: frequency counter, TIC: time-interval counter, GNSS: global navigation satellite system, y_i^{m}: fractional frequency difference between HM1′ and NMIJ-Yb1, Δy^{AOG}: fractional frequency correction applied to AOG, $\Delta y^{\mathrm{AOG}'}$: fractional frequency correction applied to AOG ′.

time difference between UTC(NMIJ) and UTC. For postprocessing generation of UTC(NMIJ)′, we compute a virtual hydrogen maser HM1′ by subtracting Δy^{AOG} from UTC(NMIJ) so that HM1′ does not have frequency steps resulting from the manual steering and thus has frequency stability mostly equivalent to that of HM1. UTC(NMIJ)′ is generated by HM1′ and another virtual AOG for steering UTC(NMIJ)′, denoted by AOG ′. The contribution of AOG to the fractional instability of UTC(NMIJ) is confirmed to be $\sim 1 \times 10^{-16}$ over an averaging time $\tau \sim 2 \times 10^6$ s, limited by measurement noise of $2 \times 10^{-10}/(\tau/\mathrm{s})$ of a time-interval counter. We expect a lower contribution of AOG according to its catalog specification [$3 \times 10^{-13}/(\tau/\mathrm{s})$].

The frequency of HM1′ is compared with that of the Yb optical lattice clock NMIJ-Yb1 [9,42,43] using an optical frequency comb [44]. The beat frequency between a laser stabilized to an ultrastable optical cavity and the comb phase locked to UTC(NMIJ) is measured by a frequency counter. The frequency of the laser is shifted by an acousto-optic modulator (AOM) and stabilized to the $^1\mathrm{S}_0$–$^3\mathrm{P}_0$ clock transition of ^{171}Yb. The beat and AOM frequencies are used to calculate the fractional frequency difference y_i^{m} between HM1′ and NMIJ-Yb1 at a time epoch i by the approximation

$$y_i^{\mathrm{m}} \sim \frac{f^{\mathrm{a}}_{\mathrm{UTC(NMIJ)}}/f^{\mathrm{a}}_{\mathrm{Yb}}}{f^{\mathrm{n}}_{\mathrm{UTC(NMIJ)}}/f^{\mathrm{n}}_{\mathrm{Yb}}} - 1 - \Delta y_i^{\mathrm{AOG}}, \tag{1}$$

where $f_{\mathrm{X}}^{\mathrm{a(n)}}$ denotes the actual (nominal) frequency of X and $\Delta y_i^{\mathrm{AOG}}$ is the correction frequency applied to AOG at epoch i. The nominal frequency is chosen as $f_{\mathrm{UTC(NMIJ)}}^{\mathrm{n}} = 10$ MHz, and $f_{\mathrm{Yb}}^{\mathrm{n}} = 518\,295\,836\,590\,863.6$ Hz, which is the CIPM (Comité International des Poids et Mesures) recommended frequency during the period of the generation of UTC(NMIJ)′ [18]. The systematic frequency shift of NMIJ-Yb1 is evaluated with a fractional uncertainty of 4.0×10^{-16} [42], and it is corrected in the calculation of y_i^{m}. The frequency stability of NMIJ-Yb1 was evaluated as $7.1 \times 10^{-15}/\sqrt{(\tau/\mathrm{s})}$ by comparing it with a Sr optical lattice clock [45–47]. The uncertainty of the comb-based frequency measurement was estimated to be 2.2×10^{-16} from the flicker noise observed when comparing two independent combs at $\tau \sim (1\text{–}5) \times 10^4$ s [42].

B. Frequency-steering scheme

In this section, we describe a scheme for the frequency steering of UTC(NMIJ)′ performed in a postprocessing analysis, but note that this scheme is also applicable to real-time generation of UTC(NMIJ)′. The frequency steering of UTC(NMIJ)′ is carried out using a Kalman filter algorithm [48] so that the frequency difference between UTC(NMIJ)′ and NMIJ-Yb1 is close to zero. The details of the Kalman filter are described in Appendix A. The Kalman filter estimates the fractional frequency offset y_i^{e} and the frequency drift d_i^{e} of HM1′ against NMIJ-Yb1 at an epoch i. For steering UTC(NMIJ)′ at a subsequent epoch $i+1$, a correction frequency $\Delta y_{i+1}^{\mathrm{Kalman}}$, which is added to the frequency of AOG ′, is determined by

$$\Delta y_{i+1}^{\mathrm{Kalman}} = -(y_i^{\mathrm{e}} + d_i^{\mathrm{e}}\,\Delta t), \tag{2}$$

where Δt denotes the time interval between epochs. Before the estimation of y_i^{e} and d_i^{e}, the Kalman filter first predicts the frequency offset y_i^{p} and the drift d_i^{p} based on y_{i-1}^{e} and d_{i-1}^{e} estimated at a previous epoch $i-1$. When the measured value y_i^{m} in Eq. (1) is available, y_i^{p} and d_i^{p} are updated to yield better estimates y_i^{e} and d_i^{e} using a weighted average of the predicted and measured values, with their weights determined based on the noise characteristics of HM1′. During the dead time of NMIJ-Yb1, this update of the predicted values is not performed.

To determine Δt and the weights to update y_i^{p} and d_i^{p}, the frequency instability of HM1′ is evaluated by comparing it with NMIJ-Yb1 before the generation of UTC(NMIJ)′, as shown in Fig. 2. To make use of the observed instability in the Kalman filter, we assume a noise model of HM1′ that approximately characterizes the Allan deviation of HM1′ with four noise parameters: $1 \times 10^{-12}/(\tau/\mathrm{s})$ for the white phase modulation (PM), $7 \times 10^{-14}/\sqrt{(\tau/\mathrm{s})}$ for the white frequency modulation (FM), 2×10^{-15} for the flicker FM, and $4 \times 10^{-24}\sqrt{(\tau/\mathrm{s})}$ for the random-walk FM. Taking account of the fact that the white PM and FM dominate at $\tau \lesssim 1 \times 10^3$ s, we choose $\Delta t = 1 \times 10^3$ s and calculate the average value of y_i^{m} over Δt. The determination of the weights to update y_i^{p} and d_i^{p} requires the estimation of the process noise and the measurement noise (see Appendix A). Here, a variance Q^{11} characterizing the process noise of the frequency offset is estimated from the flicker FM as $Q^{11} = (2 \times 10^{-15})^2$, while a variance R_i describing the measurement noise of the frequency offset is estimated by the white PM and FM, i.e., $R_i = (1 \times 10^{-12}/(\tau_i/\mathrm{s}))^2 + (7 \times 10^{-14}/\sqrt{(\tau_i/\mathrm{s})})^2$, with τ_i equal to the uptime of NMIJ-Yb1 for Δt at epoch i. The process noise of the frequency drift characterized by a variance Q^{22} is estimated as $Q^{22} = (3 \times 10^{-24}\ \mathrm{s}^{-1})^2$ based on the standard deviation of the monthly drift values of HM1 referenced to TAI for a previous year before the generation of UTC(NMIJ)′, which is provided by BIPM [13], and an assumption of a random-walk behavior $Q^{22} \propto \tau$.

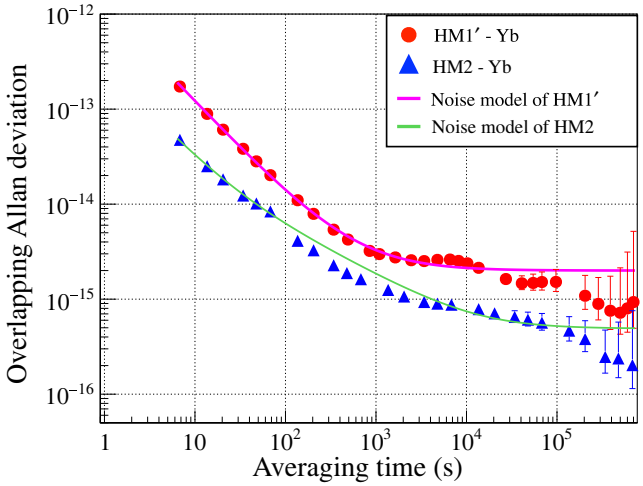

FIG. 2. Overlapping Allan deviations of HM1′ (red circles) and HM2 (blue triangles) referenced to NMIJ-Yb1. The red circles were calculated using data taken from MJD 58754 to MJD 58778 [42], and the blue triangles were obtained from MJD 60039 to MJD 60069. The error bars indicate 95% confidence intervals. The magenta and green lines indicate the noise models of HM1′ and HM2, respectively. For the generation of UTC(NMIJ)′ from MJD 58799 to MJD 59029, HM1′ was employed. The noise model of HM2 shown here was used to simulate the projected performance of UTC(NMIJ)′ (see Sec. IV).

Since the frequency of UTC is not always close to that of the SI second, frequency steering based on a primary or secondary frequency standard can increase the time difference between a steered local time scale and UTC over a long term [30]. For example, during the period of the generation of UTC(NMIJ)′, the fractional frequency offset of UTC against an ensemble of primary and secondary frequency standards, which is provided by BIPM [13], is about 5×10^{-16}, causing a time difference of -9 ns after 200 days. To address this issue, a correction frequency

$y_i^{\mathrm{UTC-Yb}}$, which approximately corresponds to the fractional frequency difference between UTC and NMIJ-Yb1, is added to $\Delta y_i^{\mathrm{Kalman}}$,

$$\Delta y_i^{\mathrm{AOG}'} = \Delta y_i^{\mathrm{Kalman}} + y_i^{\mathrm{UTC-Yb}}, \tag{3}$$

where $\Delta y_i^{\mathrm{AOG}'}$ denotes the updated correction frequency applied to AOG′. Based on discussions in Ref. [14], we determine $y_i^{\mathrm{UTC-Yb}}$ in the following method. The frequency difference between UTC and NMIJ-Yb1 averaged over a previous month is calculated based on the frequency difference between UTC and UTC(NMIJ) provided by BIPM on around the tenth day of each month [13]. This frequency-difference value between UTC and NMIJ-Yb1 is assigned to $y_i^{\mathrm{UTC-Yb}}$ in a current epoch i. Then, $y_i^{\mathrm{UTC-Yb}}$ is updated once a month when a new frequency difference between UTC and UTC(NMIJ) for a previous month is provided by BIPM.

III. RESULTS

UTC(NMIJ)′ was generated during a campaign period of 230 days from Modified Julian Date (MJD) 58799 (12 November 2019) to MJD 59029 (29 June 2020). During this period, NMIJ-Yb1 was operated with an uptime of 81.6%. Technical details regarding the robustness of NMIJ-Yb1 are described elsewhere [42,49,50]. Before the campaign, we operated NMIJ-Yb1 with an uptime of 93.9% for 24 days from MJD 58754 to MJD 58778 (i) to evaluate the noise characteristics of HM1′ and (ii) to obtain the frequency difference between UTC and NMIJ-Yb1 (see Sec. II B). The start date of MJD 58799 is set after the first correction frequency $y_i^{\mathrm{UTC-Yb}}$ is determined based on the information provided by BIPM. Figure 3(a) shows the measured y_i^{m} averaged over Δt, together with the Kalman filter estimate y_i^{e}. At MJD 58896, a large excursion of the phase of UTC(NMIJ) occurred during its maintenance, which was observed by comparing UTC(NMIJ) with another hydrogen maser HM2 (VREMYA-CH, VCH-1003M) and a commercial Cs clock. This phase excursion was measured with a time-interval counter as −78.6 ns referenced to HM2 (see Fig. 1), and it was corrected in the computation of HM1′. The frequency of HM1′ also fluctuated notably at this time, but this fluctuation was well tracked by the Kalman filter thanks to the nearly continuous operation of NMIJ-Yb1, as shown in Fig. 3(b).

To evaluate the performance of UTC(NMIJ)′, it was compared with UTC via a link based on global navigation satellite systems (GNSSs). The time difference between UTC(NMIJ)′ and UTC is obtained by the relationship (see Fig. 1)

$$\begin{aligned} x(\mathrm{UTC(NMIJ)}' - \mathrm{UTC}) = {} & x(\mathrm{UTC(NMIJ)}' - \mathrm{HM1}') \\ & + x(\mathrm{HM1}' - \mathrm{UTC(NMIJ)})) \\ & + x(\mathrm{UTC(NMIJ)} - \mathrm{UTC}), \end{aligned} \tag{4}$$

where $x(A - B)$ denotes the time difference between A and B. Since BIPM provides $x(\mathrm{UTC(NMIJ)} - \mathrm{UTC})$ at 5-day intervals [13], we calculate $x(\mathrm{UTC(NMIJ)}' - \mathrm{HM1}')$

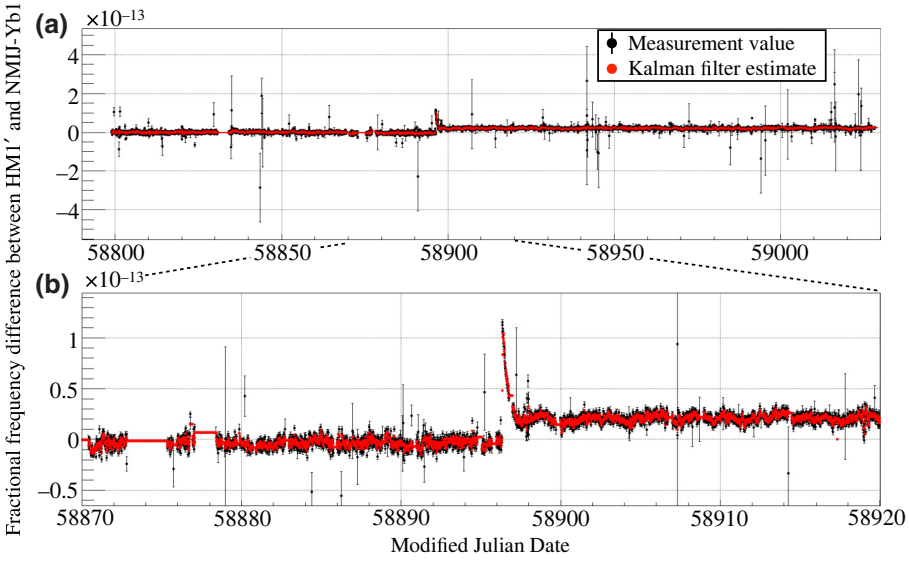

FIG. 3. Fractional frequency difference between HM1′ and NMIJ-Yb1 during (a) an entire campaign period of 230 days from MJD 58799 to MJD 59029 and (b) a specific period from MJD 58870 to MJD 58920, which shows an enlarged view of a large frequency fluctuation caused by maintenance at MJD 58896. The black points show the measured value averaged over an interval of $\Delta t = 1 \times 10^3$ s, and the red points show the values estimated by the Kalman filter. The error bars of the measured values indicate the measurement noise $\sqrt{R_i}$ used in the Kalman filter estimate, which is calculated from the white noise components of HM1′.

and $x(\mathrm{HM1}' - \mathrm{UTC(NMIJ)}))$ at the same intervals by numerically integrating the correction frequencies,

$$x(\mathrm{UTC(NMIJ)}' - \mathrm{HM1}') = \sum_{i=i_0}^{i_\mathrm{f}} \Delta y_i^{\mathrm{AOG}'} \Delta t, \qquad (5)$$

$$x(\mathrm{HM1}' - \mathrm{UTC(NMIJ)}) = -\sum_{i=i_0}^{i_\mathrm{f}} \Delta y_i^{\mathrm{AOG}} \Delta t, \qquad (6)$$

where the times at the initial and final epochs i_0 and i_f coincide with the times at which $x(\mathrm{UTC(NMIJ)} - \mathrm{UTC})$ is provided by BIPM.

Figures 4(a) and 4(b) show the results of $x(\mathrm{UTC(NMIJ)}' - \mathrm{UTC})$ during the 230-day campaign period. The behavior of our official time scale $x(\mathrm{UTC(NMIJ)} - \mathrm{UTC})$ during the same period is also shown in Fig. 4(a). It is worth noting here that NMIJ-Yb1 partially contributed to reducing the time deviation of UTC(NMIJ) from UTC at around MJD 58896 when the large frequency excursion occurred. The time difference of UTC(NMIJ)′ is significantly reduced compared with that of UTC(NMIJ). The root-mean-square difference of UTC(NMIJ)′ with respect to UTC is 0.52 ns, with a peak-to-peak difference of 2.0 ns. The maximum time deviation of UTC(NMIJ)′ from UTC is 1.1 ns.

We also analyzed the frequency stability of the obtained data of $x(\mathrm{UTC(NMIJ)}' - \mathrm{UTC})$. Figure 5 shows the overlapping Allan deviation of UTC(NMIJ)′ referenced to UTC. For comparison, the GNSS link instability [51] and the noise model of UTC [52] estimated by BIPM are also shown in Fig. 5. At $\tau \lesssim 10$ d, the Allan deviation of $x(\mathrm{UTC(NMIJ)}' - \mathrm{UTC})$ is mostly dominated by the GNSS link noise. The link noise becomes negligible at $\tau \gtrsim 10$ d due to its $1/\tau^{0.9}$ dependence [53]. During $\tau \sim 10$–40 d, the Allan deviation reaches a flicker floor of $\sim 4 \times 10^{-16}$. We attribute this floor to the instability of UTC, since the Allan deviation approximately follows the noise model of UTC. Other possibilities are discussed in Sec. IV. At $\tau \gtrsim 40$ d, the Allan deviation further decreases due to the monthly frequency adjustment of UTC(NMIJ)′ by $y_i^{\mathrm{UTC-Yb}}$ (see Sec. II B); i.e., the frequency of UTC(NMIJ)′ is locked to that of UTC in the long term.

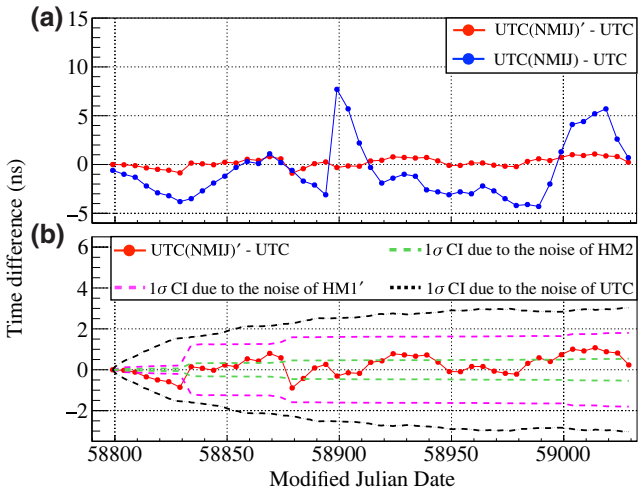

FIG. 4. (a) Time differences between UTC(NMIJ)′ (red points) and UTC(NMIJ) (blue points) from UTC. The time offset of UTC(NMIJ)′ with respect to UTC is initially set to 0 ns at MJD 58799. (b) Enlarged view of the time difference between UTC(NMIJ)′ and UTC, together with expected 1σ confidence intervals (CIs) of the time difference due to the noise of HM1′ (magenta dashed lines) and HM2 (green dashed lines) during the dead time of NMIJ-Yb1, and due to the noise of UTC with the effect of the monthly frequency adjustment (black dashed lines).

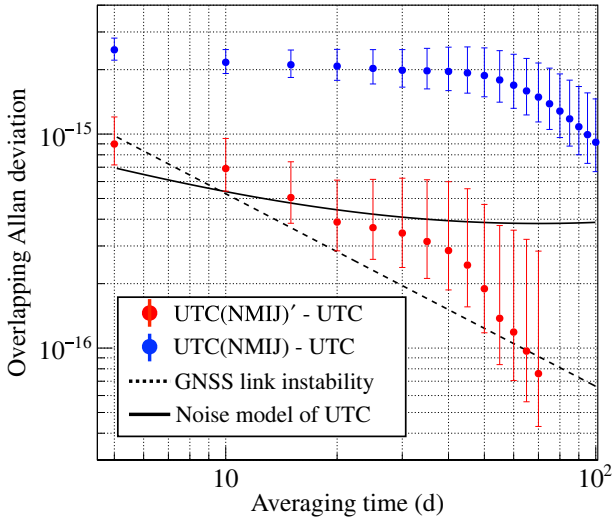

FIG. 5. Overlapping Allan deviation of UTC(NMIJ)′ referenced to UTC (red points). A typical frequency stability of UTC(NMIJ) against UTC calculated with the time-comparison data from MJD 58004 to MJD 59039 is also shown (blue points). The error bars indicate the 95% confidence intervals. The black dashed and solid lines indicate the GNSS link instability and the noise model of UTC, respectively, estimated by BIPM [51,52].

IV. DISCUSSION AND CONCLUSIONS

The performance of UTC(NMIJ)′ was compared with those of UTC(k)s in four institutes based on Cs or Rb microwave fountain clocks [14–17] operated during our 230-day campaign period; these are examples of state-of-the-art UTC(k)s generated in real time for many years. Figure 6 shows the time differences of these fountain-based UTC(k)s from UTC [13]. The root-mean-square time differences of these UTC(k)s with respect to UTC range between 0.99 and 1.6 ns, and the peak-to-peak differences are ∼3 ns. Compared with these UTC(k)s, UTC(NMIJ)′ exhibits better performance.

To estimate the effect of the dead time of NMIJ-Yb1 on the performance of UTC(NMIJ)′, we carried out a

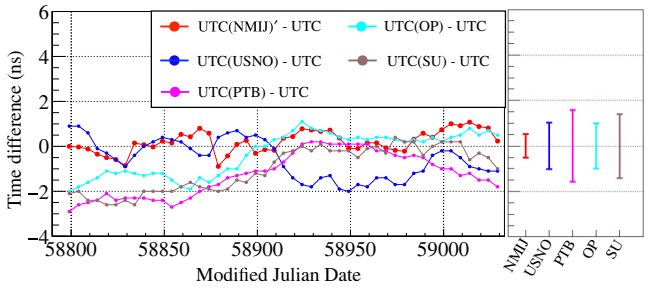

FIG. 6. Time differences of UTC(k)s from UTC during the campaign period of the generation of UTC(NMIJ)′. The error bars in the right-hand panel indicate the root-mean-square time differences of the UTC(k)s with respect to UTC. USNO: United States Naval Observatory, PTB: Physikalisch-Technische Bundesanstalt, OP: Observatoire de Paris, SU: Soviet Union.

Monte Carlo simulation of UTC(NMIJ)′ with the noise model of HM1′ (see Sec. II A) and derived the time difference of UTC(NMIJ)′ from an ideal (noiseless) reference time scale. The details of the simulation are described in Appendix B. Note that this simulation does not include the instabilities arising from NMIJ-Yb1, the comb, the GNSS link, or UTC. A 1σ confidence interval of the time difference obtained by the simulation is shown in Fig. 4(b). During the first 30 days from MJD 58799 to MJD 58829, with a high uptime of 88.3%, the absolute value of the time difference is only $\leq$0.2 ns. Over the entire campaign period, however, the 1σ confidence interval rapidly increases to a range between $\pm$1.2 ns at MJD 58834 and $\pm$1.6 ns at MJD 58879, and it finally reaches $\pm$1.8 ns at MJD 59029. The rapid changes are caused by the flicker noise of HM1′ and the prediction error of the Kalman filter during two large dead times of $\sim$3 days from MJD 58830 and $\sim$2 days from MJD 58873.

The real data x(UTC(NMIJ)′ − UTC) shown in Fig. 4(b) mostly stay within the 1σ confidence interval, but they deviate outside this interval during the first 30 days, implying that the dead time of NMIJ-Yb1 is not a dominant source that limits the stability of UTC(NMIJ)′ during this 30-day period. Since the frequency stability of the real data is expected to be limited by that of UTC during $\tau \sim$ 10–40 d (see Sec. III), it is likely that this deviation is mainly due to the instability of UTC. This is also confirmed by comparing the real data with a 1σ confidence interval calculated from the noise model of UTC [see Fig. 4(b)]. Other possibilities include the noise contributions from NMIJ-Yb1 and the comb-based measurement. The noise of NMIJ-Yb1 is assumed to be negligibly small, since the observed frequency stability of NMIJ-Yb1 reaches $\sim 1 \times 10^{-16}$ at $\tau \sim 5 \times 10^3$ s with a $1/\sqrt{\tau}$ slope [42]. The noise of the comb-based measurement may make a small contribution if the observed flicker noise of 2.2×10^{-16} at $\tau \sim$ (1–5) $\times 10^4$ s (see Sec. II A) is still dominant at $\tau \sim$ 30 d.

With a better flywheel oscillator, unprecedented performance of UTC(NMIJ)′ is expected thanks to the high uptime of NMIJ-Yb1. To demonstrate this, we carried out another Monte Carlo simulation using a noise model of HM2 exhibiting better frequency stability: $3 \times 10^{-13}/(\tau/\mathrm{s})$ for the white PM, $6 \times 10^{-14}/\sqrt{(\tau/\mathrm{s})}$ for the white FM, 5×10^{-16} for the flicker FM, and $2 \times 10^{-27}\sqrt{(\tau/\mathrm{s})}$ for the random-walk FM (see Fig. 2). The frequency stability of HM2 was evaluated against NMIJ-Yb1 after the campaign by establishing a direct link between NMIJ-Yb1 and HM2. We note that HM2 was not employed as a flywheel oscillator during the campaign, since the frequency stability of the comparison between HM2 and NMIJ-Yb1 was heavily degraded by measurement noise from a time-interval counter (see Fig. 1). With the same uptime of NMIJ-Yb1 (81.6% over 230 days), the absolute value of the time difference obtained with the model of HM2 is only $\leq$0.06 ns during the first 30 days and $\leq$0.54 ns over the entire 230-day period, as shown in Fig. 4(b). The performance during the first 30 days is comparable to a reported time error of 48 ± 94 ps against an ideal reference for 34 days achieved by an all-optical time scale based on a cryogenic silicon cavity [36].

When the instability arising from the noise of HM2 during the dead time of NMIJ-Yb1 reaches this level, the other noise sources will limit the performance of UTC(NMIJ)′. The dominant sources are expected to be the GNSS link and UTC, as long as UTC(NMIJ)′ is compared with UTC in the current infrastructure. Considering the stability of UTC(NMIJ)′ itself, it may be limited by the noise of NMIJ-Yb1 and of the comb-based measurement. We have already reduced some of the noise in more recent investigations [9,54] and plan to achieve the stability level estimated by the simulation in the future.

In conclusion, we have generated UTC(NMIJ)′ for 230 days by steering the frequency of a single hydrogen maser to that of NMIJ-Yb1 running nearly continuously. UTC(NMIJ)′ exhibits a lower time difference with respect to UTC compared with those of other UTC(k)s based on Cs or Rb fountain clocks. We have demonstrated that the use of an optical clock with a high uptime enhances the stability of a time scale. This work constitutes an essential step toward a redefinition of the SI second.

Note added.—Recently, we became aware of another report on the generation of a time scale based on a hydrogen maser steered by an Yb optical lattice clock, which shows subnanosecond accuracy over month-long periods and nanosecond accuracy over a 1-year period with respect to UTC [55].

ACKNOWLEDGMENTS

We are indebted to A. Iwasa and Y. Fujii for the support to maintain UTC(NMIJ). We thank the BIPM time department for making the data available on their

website. This work was supported by the Japan Society for the Promotion of Science (JSPS) KAKENHI Grant Nos. 17H01151, 17K14367, and 22H01241, the JST-Mirai Program Grant No. JPMJMI18A1, and the JST Moonshot R & D Program Grant No. JPMJMS2268, Japan.

APPENDIX A: KALMAN FILTER ALGORITHM

We employ a Kalman filter algorithm similar to that described in Ref. [48]. The Kalman filter estimates the frequency offset y_i^{e} and the frequency drift d_i^{e} of the hydrogen maser against NMIJ-Yb1 at a time epoch i with a time interval Δt to yield the correction frequency applied to AOG′ at a subsequent epoch $i+1$ [see Eq. (2)]. Before y_i^{e} and d_i^{e} are determined, the Kalman filter predicts the frequency offset y_i^{p} and the drift d_i^{p} based on y_{i-1}^{e} and d_{i-1}^{e} estimated at a previous epoch $i-1$ by

$$\begin{pmatrix} y_i^{\mathrm{p}} \\ d_i^{\mathrm{p}} \end{pmatrix} = \begin{pmatrix} 1 & \Delta t \\ 0 & 1 \end{pmatrix} \begin{pmatrix} y_{i-1}^{\mathrm{e}} \\ d_{i-1}^{\mathrm{e}}. \end{pmatrix}. \tag{A1}$$

During the dead time of NMIJ-Yb1, the predicted values are simply used for y_i^{e} and d_i^{e}, i.e.,

$$\begin{pmatrix} y_i^{\mathrm{e}} \\ d_i^{\mathrm{e}} \end{pmatrix} = \begin{pmatrix} y_i^{\mathrm{p}} \\ d_i^{\mathrm{p}} \end{pmatrix}. \tag{A2}$$

When the frequency offset y_i^{m} measured using NMIJ-Yb1 is available, the predicted values are updated by a weighted average of the predicted and measured values as follows:

$$\begin{pmatrix} y_i^{\mathrm{e}} \\ d_i^{\mathrm{e}} \end{pmatrix} = \begin{pmatrix} y_i^{\mathrm{p}} \\ d_i^{\mathrm{p}} \end{pmatrix} + K_i (y_i^{\mathrm{m}} - y_i^{\mathrm{p}}), \tag{A3}$$

where K_i is the Kalman gain matrix, which determines the weights of the predicted and measured values. In the present model, with the frequency offset and the drift as described in Eq. (A1), the Kalman gain matrix is given by

$$\begin{aligned} K_i &= \begin{pmatrix} K_i^y \\ K_i^d \end{pmatrix} \\ &= \begin{pmatrix} \dfrac{p_i^{11} + \Delta t(p_i^{21} + p_i^{12} + \Delta t p_i^{22}) + Q^{11}}{p_i^{11} + \Delta t(p_i^{21} + p_i^{12} + \Delta t p_i^{22}) + Q^{11} + R_i} \\ \dfrac{p_i^{21} + \Delta t p_i^{22}}{p_i^{11} + \Delta t(p_i^{21} + p_i^{12} + \Delta t p_i^{22}) + Q^{11} + R_i} \end{pmatrix}, \end{aligned} \tag{A4}$$

where Q^{11} and R_i are variances characterizing the process noise and the measurement noise of the frequency offset, respectively. Further, $p_i^{11}, p_i^{12}, p_i^{21}$, and p_i^{22} are elements of a covariance matrix P_i of the estimate, defined as

$$P_i = \begin{pmatrix} p_i^{11} & p_i^{12} \\ p_i^{21} & p_i^{22} \end{pmatrix}, \tag{A5}$$

and these are obtained from P_{i-1} and K_{i-1} at the previous epoch $i-1$ by

$$\begin{aligned} p_i^{11} &= \left(1 - K_{i-1}^y\right)\left[p_{i-1}^{11} + \Delta t\left(p_{i-1}^{21} + p_{i-1}^{12} + \Delta t p_{i-1}^{22}\right) + Q^{11}\right], \\ p_i^{12} &= \left(1 - K_{i-1}^y\right)\left(p_{i-1}^{12} + \Delta t p_{i-1}^{22}\right), \\ p_i^{21} &= p_{i-1}^{21} + \Delta t p_{i-1}^{22} \\ &\quad - K_{i-1}^d\left[p_{i-1}^{11} + \Delta t\left(p_{i-1}^{21} + p_{i-1}^{12} + \Delta t p_{i-1}^{22}\right) + Q^{11}\right], \\ p_i^{22} &= p_{i-1}^{22} - K_{i-1}^d\left(p_{i-1}^{12} + \Delta t p_{i-1}^{22}\right) + Q^{22}, \end{aligned} \tag{A6}$$

where Q^{22} is a variance characterizing the process noise of the drift. The execution of the Kalman filter algorithm requires the determination of Q^{11}, Q^{22}, and R_i by the user. We estimate these variances based on the measured noise characteristics of the hydrogen maser (see Sec. II B).

APPENDIX B: MONTE CARLO SIMULATION

In the Monte Carlo simulation, we generate time-series data of the frequency with a power spectral density that is converted from the Allan deviation characterized by the noise model of HM1′ or HM2 [56]. The frequency data are then gapped according to the dead time of NMIJ-Yb1. With the same Kalman filter algorithm, the frequency of HM1′ or HM2 is estimated from the gapped data. By integrating the frequency difference between the frequency estimated by the Kalman filter and the true frequency obtained from the data without the gap, the time difference between the simulated UTC(NMIJ)′ and an ideal time scale is obtained. We repeat this procedure 200 times and calculate the root-mean-square values of the time differences, which are the 1σ confidence intervals of the time differences shown in Fig. 4(b).

For calculation of the 1σ confidence interval due to the noise of UTC, we generate another Monte Carlo simulation dataset of the frequency based on the noise model of UTC [52]. To include the effect of the monthly frequency adjustment of UTC(NMIJ)′ by $y_i^{\mathrm{UTC-Yb}}$ (see Sec. II B), a correction frequency is similarly calculated approximately once a month by averaging simulated frequencies over a previous month, and this is added to a simulated frequency at a current time epoch. The resulting frequencies are integrated to obtain the time difference between UTC and an ideal time scale.

[1] T. Takano, M. Takamoto, I. Ushijima, N. Ohmae, T. Akatsuka, A. Yamaguchi, Y. Kuroishi, H. Munekane, B. Miyahara, and H. Katori, Geopotential measurements with synchronously linked optical lattice clocks, Nat. Photonics **10**, 662 (2016).

[2] J. Grotti, S. Koller, S. Vogt, S. Häfner, U. Sterr, C. Lisdat, H. Denker, C. Voigt, L. Timmen, and A. Rolland *et al.*, Geodesy and metrology with a transportable optical clock, Nat. Phys. **14**, 437 (2018).

[3] A. Hees, J. Guéna, M. Abgrall, S. Bize, and P. Wolf, Searching for an oscillating massive scalar field as a dark matter candidate using atomic hyperfine frequency comparisons, Phys. Rev. Lett. **117**, 061301 (2016).

[4] P. Wcisło, P. Ablewski, K. Beloy, S. Bilicki, M. Bober, R. Brown, R. Fasano, R. Ciuryło, H. Hachisu, and T. Ido *et al.*, New bounds on dark matter coupling from a global network of optical atomic clocks, Sci. Adv. **4**, eaau4869 (2018).

[5] N. Ashby, T. E. Parker, and B. R. Patla, A null test of general relativity based on a long-term comparison of atomic transition frequencies, Nat. Phys. **14**, 822 (2018).

[6] C. J. Kennedy, E. Oelker, J. M. Robinson, T. Bothwell, D. Kedar, W. R. Milner, G. E. Marit, A. Derevianko, and J. Ye, Precision metrology meets cosmology: Improved constraints on ultralight dark matter from atom-cavity frequency comparisons, Phys. Rev. Lett. **125**, 201302 (2020).

[7] M. Takamoto, I. Ushijima, N. Ohmae, T. Yahagi, K. Kokado, H. Shinkai, and H. Katori, Test of general relativity by a pair of transportable optical lattice clocks, Nat. Photonics **14**, 411 (2020).

[8] R. Lange, N. Huntemann, J. M. Rahm, C. Sanner, H. Shao, B. Lipphardt, Chr. Tamm, S. Weyers, and E. Peik, Improved limits for violations of local position invariance from atomic clock comparisons, Phys. Rev. Lett. **126**, 011102 (2021).

[9] T. Kobayashi, A. Takamizawa, D. Akamatsu, A. Kawasaki, A. Nishiyama, K. Hosaka, Y. Hisai, M. Wada, H. Inaba, T. Tanabe, and M. Yasuda, Search for ultralight dark matter from long-term frequency comparisons of optical and microwave atomic clocks, Phys. Rev. Lett. **129**, 241301 (2022).

[10] M. Filzinger, S. Dörscher, R. Lange, J. Klose, M. Steinel, E. Benkler, E. Peik, C. Lisdat, and N. Huntemann, Improved limits on the coupling of ultralight bosonic dark matter to photons from optical atomic clock comparisons, Phys. Rev. Lett. **130**, 253001 (2023).

[11] A. Sherrill, A. O. Parsons, C. F. A. Baynham, W. Bowden, E. A. Curtis, R. Hendricks, I. R. Hill, R. Hobson, H. S. Margolis, B. I. Robertson, M. Schioppo, K. Szymaniec, A. Tofful, J. Tunesi, R. M. Godun, and X. Calmet, Analysis of atomic-clock data to constrain variations of fundamental constants, New J. Phys. **25**, 093012 (2023).

[12] G. Panfilo and F. Arias, The Coordinated Universal Time (UTC), Metrologia **56**, 042001 (2019).

[13] FTP server of the BIPM Time Department, https://www.bipm.org/en/time-ftp.

[14] A. Bauch, S. Weyers, D. Piester, E. Staliuniene, and W. Yang, Generation of UTC(PTB) as a fountain-clock based time scale, Metrologia **49**, 180 (2012).

[15] Y. S. Domnin, V. N. Baryshev, A. I. Boyko, G. A. Elkin, A. V. Novoselov, L. N. Kopylov, and D. S. Kupalov, The MTsR-F2 fountain-type cesium frequency standard, Meas. Tech. **55**, 1155 (2013).

[16] S. Peil, J. L. Hanssen, T. B. Swanson, J. Tayler, and C. R. Ekstrom, Evaluation of long term performance of continuously running atomic fountains, Metrologia **51**, 263 (2014).

[17] G. D. Rovera, S. Bize, B. Chupin, J. Guéna, P. Laurent, P. Rosenbusch, P. Uhrich, and M. Abgrall, UTC(OP) based on LNE-SYRTE atomic fountain primary frequency standards, Metrologia **53**, S81 (2016).

[18] F. Riehle, P. Gill, F. Arias, and L. Robertsson, The CIPM list of recommended frequency standard values: Guidelines and procedures, Metrologia **55**, 188 (2018).

[19] F.-L. Hong, Optical frequency standards for time and length applications, Meas. Sci. Technol. **28**, 012002 (2016).

[20] N. Dimarcq, M. Gertsvolf, G. Mileti, S. Bize, C. W. Oates, E. Peik, D. Calonico, T. Ido, P. Tavella, and F. Meynadier *et al.*, Roadmap towards the redefinition of the second, Metrologia **61**, 012001 (2024).

[21] T. Bothwell, D. Kedar, E. Oelker, J. M. Robinson, S. L. Bromley, W. L. Tew, J. Ye, and C. J. Kennedy, JILA SrI optical lattice clock with uncertainty of 2.0×10^{-18}, Metrologia **56**, 065004 (2019).

[22] I. Ushijima, M. Takamoto, M. Das, T. Ohkubo, and H. Katori, Cryogenic optical lattice clocks, Nat. Photonics **9**, 185 (2015).

[23] N. Huntemann, C. Sanner, B. Lipphardt, C. Tamm, and E. Peik, Single-ion atomic clock with 3×10^{-18} systematic uncertainty, Phys. Rev. Lett. **116**, 063001 (2016).

[24] W. F. McGrew, X. Zhang, R. J. Fasano, S. A. Schäffer, K. Beloy, D. Nicolodi, R. C. Brown, N. Hinkley, G. Milani, M. Schioppo, T. H. Yoon, and A. D. Ludlow, Atomic clock performance enabling geodesy below the centimetre level, Nature **564**, 87 (2018).

[25] S. M. Brewer, J.-S. Chen, A. M. Hankin, E. R. Clements, C. W. Chou, D. J. Wineland, D. B. Hume, and D. R. Leibrandt, $^{27}Al^{+}$ Quantum-logic clock with a systematic uncertainty below 10^{-18}, Phys. Rev. Lett. **123**, 033201 (2019).

[26] Y. Hung, B. Zhang, M. Zeng, Y. Hao, Z. Ma, H. Zhang, H. Guan, Z. Chen, M. Wang, and K. Gao, Liquid-nitrogen-cooled Ca^{+} optical clock with systematic uncertainty of 3×10^{-18}, Phys. Rev. Appl. **17**, 034041 (2022).

[27] A. Zhang, Z. Xiong, X. Chen, Y. Jiang, J. Wang, C. Tian, Q. Zhu, B. Wang, D. Xiong, L. He, L. Ma, and B. Lyu, Ytterbium optical lattice clock with instability of order 10^{-18}, Metrologia **59**, 065009 (2022).

[28] Z. Zhiqiang, K. J. Arnold, R. Kaewuam, and M. D. Barrett, $^{176}Lu^{+}$ clock comparison at the 10^{-18} level via correlation spectroscopy, Sci. Adv. **9**, eadg1971 (2023).

[29] C. Grebing, A. Al-Masoudi, S. Dörsher, S. Häfner, V. Gerginov, S. Weyers, B. Lipphardt, F. Riehle, U. Sterr, and C. Lisdat, Realization of a timescale with an accurate optical lattice clock, Optica **3**, 563 (2016).

[30] H. Hachisu, F. Nakagawa, Y. Hanado, and T. Ido, Months-long real-time generation of a time scale based on an optical clock, Sci. Rep. **8**, 4243 (2018).

[31] J. Yao, J. A. Sherman, T. Fortier, H. Leopardi, T. Parker, W. McGrew, X. Zhang, D. Nicolodi, R. Fasano, and S. Schäffer *et al.*, Optical-clock-based time scale, Phys. Rev. Appl. **12**, 044069 (2019).

[32] V. Formichella, L. Galleani, G. Signorille, and I. Sesia, Robustness tests for an optical time scale, Metrologia **59**, 015002 (2022).

[33] L. Zhu, Y. Lin, Y. Wang, Z. Jia, Q. Wang, Y. Li, T. Yang, and Z. Fang, Preliminary study of generating a local time scale with NIM ^{87}Sr optical lattice clock, Metrologia **59**, 055007 (2022).

[34] H. S. Lee, T. Y. Kwon, S. E. Park, Y. K. Lee, S.-h. Yang, D.-H. Yu, M.-S. Heo, H. Kim, C. Y. Park, and W.-K. Lee, Characteristics of a real-time ensemble time scale corrected by the KRISS-PSFS using a reduced Kalman filter (Kred) algorithm, Metrologia **60**, 045006 (2023).

[35] Q. Xu, S. Wang, X. Lu, F. Guo, J. Xia, Y. Wang, and H. Chang, Demonstration of a time scale with the ^{87}Sr optical lattice clock at NTSC, AIP Adv. **13**, 115316 (2023).

[36] W. R. Milner, J. M. Robinson, C. J. Kennedy, T. Bothwell, D. Kedar, D. G. Matei, T. Legero, U. Sterr, F. Riehle, H. Leopardi, T. M. Fortier, J. A. Sherman, J. Levine, J. Yao, J. Ye, and E. Melker, Demonstration of a timescale based on a stable optical carrier, Phys. Rev. Lett. **123**, 173201 (2019).

[37] I. R. Hill, R. Hobson, W. Bowden, E. M. Bridge, S. Donnellan, E. A. Curtis, and P. Gill, A low maintenance Sr optical lattice clock, J. Phys. Conf. Ser. **723**, 012019 (2016).

[38] J. Lodewyck, S. Bilicki, E. Bookjans, J.-L. Robyr, C. Shi, G. Vallet, R. L. Targat, D. Nicolodi, Y. Coq, J. Guéna, M. Abgrall, P. Rosenbusch, and S. Bize, Optical to microwave clock frequency ratios with a nearly continuous strontium optical lattice clock, Metrologia **53**, 1123 (2016).

[39] C. F. Baynham, R. M. Godun, J. M. Jones, S. A. King, P. B. R. Nisbet-Jones, F. Baynes, A. Rolland, P. E. G. Baird, K. Bongs, P. Gill, and H. S. Margolis, Absolute frequency measurement of the $^2S_{1/2} \rightarrow {}^2F_{7/2}$ optical clock transition in $^{171}Yb^+$ with an uncertainty of 4×10^{-16} using a frequency link to international atomic time, J. Mod. Opt. **65**, 585 (2017).

[40] J. Stuhler, M. Abdel Hafiz, B. Arar, A. Bawamia, K. Bergner, M. Biethahn, S. Brakhane, A. Didier, J. Fortágh, and M. Halder *et al.*, Opticlock: Transportable and easy-to-operate optical single-ion clock, Meas.: Sens. **18**, 100264 (2021).

[41] M. Zeng, Y. Huang, B. Zhang, Y. Hao, Z. Ma, R. Hu, H. Zhang, Z. Chen, M. Wang, H. Guan, and K. Gao, Toward a transportable Ca^+ optical clock with a systematic uncertainty of 4.8×10^{-18}, Phys. Rev. Appl. **19**, 064004 (2023).

[42] T. Kobayashi, D. Akamatsu, K. Hosaka, Y. Hisai, M. Wada, H. Inaba, T. Suzuyama, F.-L. Hong, and M. Yasuda, Demonstration of the nearly continuous operation of an ^{171}Yb optical lattice clock for half a year, Metrologia **57**, 065021 (2020).

[43] T. Kobayashi, D. Akamatsu, Y. Hisai, T. Tanabe, H. Inaba, T. Suzuyama, F.-L. Hong, K. Hosaka, and M. Yasuda, Uncertainty evaluation of an ^{171}Yb optical lattice clock at NMIJ, IEEE Trans. Ultrason., Ferroelectr., Freq. Control **65**, 2449 (2018).

[44] H. Inaba, Y. Daimon, F.-L. Hong, A. Onae, K. Minoshima, T. R. Schibli, H. Matsumoto, M. Hirano, T. Okuno, M. Onishi, and M. Nakazawa, Long-term measurement of optical frequencies using a simple, robust and low-noise fiber based frequency comb, Opt. Express **14**, 5223 (2006).

[45] D. Akamatsu, H. Inaba, K. Hosaka, M. Yasuda, A. Onae, T. Suzuyama, M. Amemiya, and F.-L. Hong, Spectroscopy and frequency measurement of the ^{87}Sr clock transition by laser linewidth transfer using an optical frequency comb, Appl. Phys. Express **7**, 012401 (2013).

[46] Y. Hisai, D. Akamatsu, T. Kobayashi, K. Hosaka, H. Inaba, F.-L. Hong, and M. Yasuda, Improved frequency ratio measurement with ^{87}Sr and ^{171}Yb optical lattice clocks at NMIJ, Metrologia **58**, 015008 (2021).

[47] The frequency stability observed in the comparison between the Yb and Sr optical lattice clocks is $\sigma_{\mathrm{Yb/Sr}} = 1.0 \times 10^{-14}/\sqrt{(\tau/\mathrm{s})}$. The frequency stability of the Yb optical lattice clock is derived by $\sigma_{\mathrm{Yb/Sr}}/\sqrt{2}$ assuming that both clocks have the same frequency stabilities.

[48] J. Yao, T. E. Parker, N. Ashby, and J. Levine, Incorporating an optical clock into a time scale, IEEE Trans. Ultrason., Ferroelectr., Freq. Control **65**, 127 (2018).

[49] Y. Hisai, D. Akamatsu, T. Kobayashi, S. Okubo, H. Inaba, K. Hosaka, M. Yasuda, and F.-L. Hong, Development of 8-branch Er:Fiber frequency comb for Sr and Yb optical lattice clocks, Opt. Express **27**, 6404 (2019).

[50] T. Kobayashi, D. Akamatsu, K. Hosaka, and M. Yasuda, A relocking scheme for optical phase locking using a digital circuit with an electrical delay line, Rev. Sci. Instrum. **90**, 103002 (2019).

[51] The GNSS link instability is derived from a recommended formula to calculate the satellite link uncertainty $u_{\mathrm{link}} = (\sqrt{2}u_{\mathrm{A}})/(86\,400 \times 5\ \mathrm{s})(((\tau/\mathrm{d})/5))^{0.9}$ with the statistical uncertainty $u_{\mathrm{A}} = 0.3$ ns [13,53].

[52] The noise model of UTC referenced to the SI second is as follows: $1.4 \times 10^{-15}/\sqrt{(\tau/\mathrm{d})}$ for the white FM, 3×10^{-16} for the flicker FM, and $2 \times 10^{-17}\sqrt{(\tau/\mathrm{d})}$ for the random-walk FM [13]. While BIPM provides this model for the Echelle Atomique Libre (EAL), which corresponds to a flywheel oscillator for TAI and UTC, the frequency offset between EAL and UTC was constant during the campaign period (i.e., frequency steering of UTC was not performed), and thus the frequency stability of EAL is equivalent to that of UTC.

[53] G. Panfilo and T. E. Parker, A theoretical and experimental analysis of frequency transfer uncertainty, including frequency transfer into TAI, Metrologia **47**, 552 (2010).

[54] M. Wada and H. Inaba, Femtosecond-comb based 10 MHz-to-optical frequency link with uncertainty at the 10^{-18} level, Metrologia **59**, 065005 (2022).

[55] V. Formichella, G. Signorile, T. T. Thai, L. Galleani, M. Pizzocaro, I. Goti, S. Condio, C. Clivati, M. Risaro, F. Levi, D. Calonico, and I. Sesia, Year-long optical time scale with sub-nanosecond capabilities, Optica **11**, 523 (2024).

[56] W. Riley, *Handbook of Frequency Stability Analysis* (NIST Special Publication, Washington DC, 2008), Vol. 1065.